



Compressive Behavior of Isogrid Columns Fabricated with Bend-Forming

Harsh Bhundiya*, Fabien Royer†, and Zachary Cordero‡
Massachusetts Institute of Technology, Cambridge, MA, 02139

In this study, isogrid columns used in various space applications are made using a novel in-space manufacturing process termed Bend-Forming. The process uses a machine that bends a continuous strand of wire at specific locations, to form a flat lattice. Several straight wire members are attached at the bend locations using 3D-printed joints, and the lattice is then rolled to form a 3D column. Four columns with varying geometric parameters are fabricated. Compression tests are conducted on these columns, and their buckling and post-buckling behavior is investigated. These experiments show that the structures undergo a smooth formation of buckling deformations, and that contrary to thin-shell columns, they do not exhibit an abrupt destabilization past their first bifurcation. A finite element model is then implemented and numerical results are compared to the experimental responses. The comparison highlights the importance of the joint compliance in the initial response of the structure and identifies the need for modeling softer joints. Nonetheless, the model accurately predicts the maximum loads the columns can withstand and highlights the imperfection-insensitive nature of these structures, as compared to conventional shell structures.

I. Nomenclature

E	=	Young's Modulus, GPa
H	=	column height, m
D	=	column diameter, m
SL	=	triangle side length, m
ν	=	Poisson ratio

II. Introduction

There is presently resurgent interest in constructing large space structures via in-space manufacturing techniques (ISM) which form raw feedstock materials into structures on orbit. ISM offers the unique opportunity for on-demand fabrication of structures optimized for the space environment, potentially enabling larger designs than with conventional deployable structures. A variety of ISM methods have been proposed for space, such as additive manufacturing of structures from metallic or fiber-reinforced composites[1]; thermoplastic extrusion of CFRP trusses [2, 3]; and deformation processing of trusses through plastic deformation [4]. A recent analysis comparing these proposed ISM methods [5] shows that deformation processing of metallic feedstock has the lowest specific energy consumption and can thus achieve fast build rates on orbit, making it an attractive manufacturing method for space.

Motivated by this analysis, here we focus on a specific deformation process for space, termed Bend-Forming, which uses CNC wire-bending and self-locking joints to form a continuous wire into lightweight truss structures. To fabricate larger trusses from wire feedstock via Bend-Forming, a bend path comprising a sequence of straight sections and bends is prescribed to the wire bending machine, such that the straight sections serve as truss members and the bends serve as truss nodes. Joints are then placed at the nodes to hold the wire, resulting in a stiff truss structure. Fig. 1 shows exemplar reticulated shell structures fabricated with Bend-Forming.

An understanding of the structural response of Bend-Formed shells is essential to designing and manufacturing optimal truss structures. The reticulated trusses fabricated with Bend-Forming are made of continuous wire with

*Graduate Student, Department of Aeronautics and Astronautics, 77 Massachusetts Avenue, Cambridge, MA 02139, AIAA Student Member

†Postdoctoral Researcher, Department of Aeronautics and Astronautics, 77 Massachusetts Avenue, Cambridge, MA 02139, AIAA Member

‡Boeing Assistant Professor, Department of Aeronautics and Astronautics, 77 Massachusetts Avenue, Cambridge, MA 02139, AIAA Member

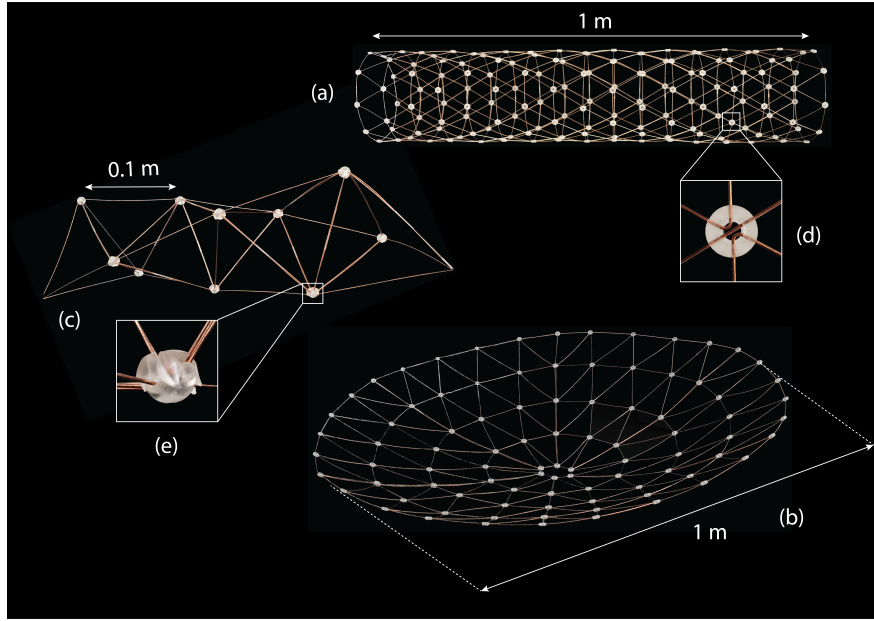


Fig. 1 Exemplar Bend-Formed structures: (a) isogrid column, (b) curved reticulated shell, and (c) tetrahelix truss. Each prototype is made from a single, continuous wire with a CNC wire bending machine [6]. The nodes consist of 3D printed joints (d, e) which snap together to hold the wire.

localized bends and held together with mechanical joints, which presents interesting challenges in modeling load transfer and predicting strength. Extensive analyses of reticulated shells have been pursued by the civil engineering community, for applications such as large roof structures [7] and domes [8]. In addition, reticulated columns have previously been studied theoretically [9–12] and experimentally [13] using the isotropic properties of a flat lattice to predict their axial, bending, and torsional stiffnesses, as well as their buckling load. In [9], for instance, the author derived minimal mass designs for isogrid columns subjected to compressive loads by using equivalent axial and bending stiffnesses of a flat triangular lattice with square cross-section members. Other studies, [10] and [11], have investigated the validity of using isotropic continuum properties for reticulated structures by comparing an equivalent shell analysis with a discrete structural description which models each member separately. In [10], the authors analytically derived buckling loads for a reticulated spherical cap and an infinite reticulated cylinder made of an equilateral triangular grid, using both continuum isotropic properties and a discrete analysis. They found that the continuum analysis overpredicts the buckling load when the characteristic buckling wavelength is on the order of the member length, or when the axial load in the members is on the order of their simply-supported Euler buckling load. Another study [11] compared the axial, flexural, and torsional stiffnesses of reticulated columns with both an equivalent continuum analysis and finite element models. They found that the effective in-plane properties accurately predict the column stiffnesses for a triangular lattice, but they result in an overprediction for other geometries like the Kagome lattice. While these previous studies focused on reticulated columns made of straight members, another experimental study [13] considered the effect of initial member imperfections on the buckling response. In particular, the authors investigated the effect of the initial curvature of the members and derived a relationship between imperfection amplitude and reduction in stiffness, which matched with experimental results in compression, bending, and torsion.

In the work presented here, Bend-Formed isogrid columns are manufactured by rolling a flat triangular wire lattice, which results in initially curved and prestressed members, as described in Section III.A. While the overall column geometry resembles the reticulated columns previously studied, the initial curvature of the members significantly complicates the analysis of their mechanical behavior, as each member undergoes 3D deformations even before buckling. This paper investigates the compressive behavior of such columns (Fig. 1a) through experimental and numerical analyses. In particular, experiments reveal the columns complex buckling and post-buckling behavior, which is further analyzed using finite element simulations including initial prestress and curvature of the members. Through this work, we generate a framework for predicting the strength of Bend-Formed columns, and identify future research avenues to improve their design and analysis.

III. Methods

A. Fabrication of Isogrid Columns

Bend-Forming uses a bend path consisting of a sequence of straight sections and bends to construct trusses from continuous feedstock. For minimum mass designs, this continuous bend path is computed with route inspection algorithms, which find the shortest closed path which visits each edge of the truss (i.e., an Euler path). An efficient algorithm for computing such paths is the Hierholzer algorithm [14], which concatenates various closed loops to form a continuous path through the truss. The Hierholzer algorithm finds Euler paths for trusses with even connectivity at each node, and can also be applied to arbitrary trusses by adding duplicate edges until each node has even connectivity. Since the necessary condition for rigidity of large pin-jointed trusses also requires an even connectivity at each node ($Z=6$ in 2D and $Z=12$ in 3D) [15], continuous wire bend paths generated with this process can fabricate rigid trusses with zero mechanisms and zero states of self-stress.

Here we use this path-planning process to generate bend paths for an isogrid column parameterized by its diameter D , height H , and triangle side length SL . Starting with the 3D column geometry (Fig. 2a), we recognize each node has even connectivity ($Z=6$), so the Hierholzer algorithm can be implemented without adding additional edges to the truss. However, for compatibility with a wire bending machine which has only two degrees of freedom, we first unroll the geometry about a spiral edge depicted in red. The resulting 2D unrolled geometry (Fig. 2b) has even connectivity at all nodes except two nodes which serve as the start and end points of a continuous bend path. The Hierholzer algorithm is then used to find a continuous bend path which traverses the truss geometry. While the Hierholzer algorithm generates a continuous bend path at random, here we select a particular zigzag path (Fig. 2c) which traverses each longeron of the column separately, to avoid wire overlaps and allow for ease of fabrication. Once generated, the bend path is converted to a series of feed/bend instructions for the wire bending machine and used to fabricate the 2D unrolled geometry of Figure 2b.

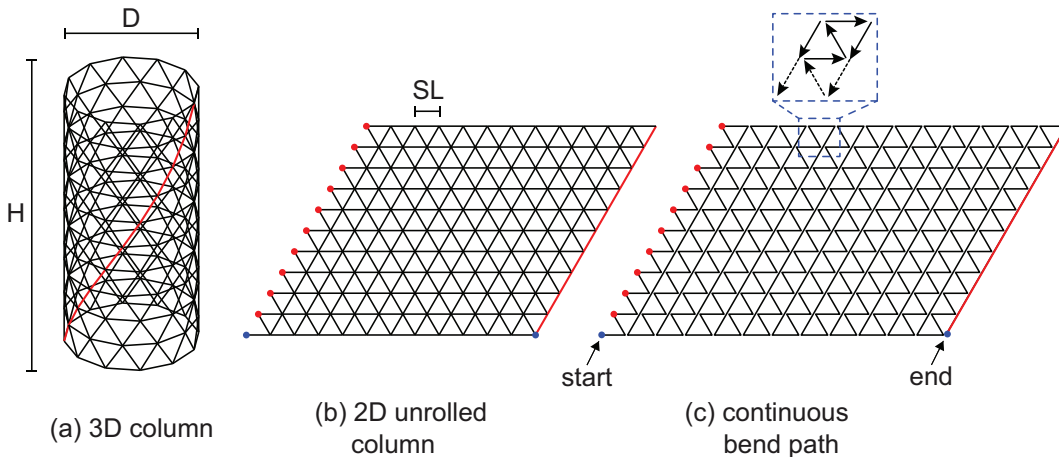


Fig. 2 Path-planning process for an isogrid column parametrized by its diameter D , height H , and triangle side length SL . (a) The 3D column is unrolled about a spiral edge highlighted in red. (b) The unrolled geometry has even connectivity at each node except two nodes highlighted in blue. (c) A continuous bend path, which starts and ends at the two blue nodes, is then found using the Hierholzer algorithm.

Once the unrolled geometry has been constructed with the wire bending machine, mechanical joints are placed at each node to hold the wire feedstock and provide stiffness. In this work we used 3D-printed plastic joints, shown in Fig. 3, to clamp the wire. The joints have two parts: a bottom part with grooves which position the wire and a top part with pins which snap into holes in the bottom part. Once snapped together around the wire at each node (Fig 3b), the joints facilitate load transfer between adjacent struts and provide stiffness to the truss.

The final step for fabricating an isogrid column is to roll the 2D geometry to achieve the 3D column of Fig. 2a. We achieve this by bending the flat, unrolled geometry about the axis of the cylinder and merging the leftmost and rightmost nodes together with a final set of joints.

We used this process to fabricate four isogrid columns with varying diameter, height, and sidelength. Table 1 lists the geometrical parameters, total wire length, and number of bends for each column; and Fig. 4 shows the fabricated

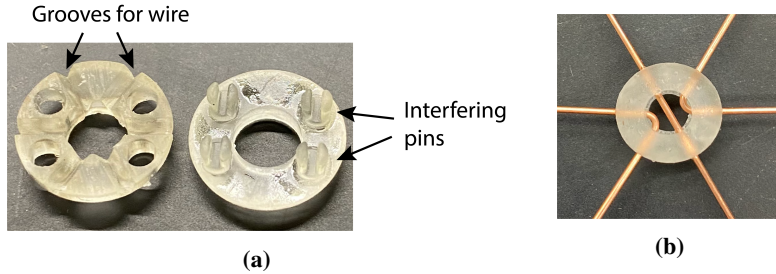


Fig. 3 (a) Close-up of joint geometry with top and bottom parts and (b) attached joint.

Column	D (mm)	H (mm)	Side length (mm)	Total wire length (m)	Total number of bends
Baseline	210 ± 3	562 ± 2	82.5	16.5	143
Small side length	206 ± 3	569 ± 2	65	20.2	219
Wide	259 ± 3	562 ± 2	82.5	20.5	179
Long	206 ± 3	850 ± 2	82.5	24.75	207

Table 1 Geometrical and fabrication parameters for the four isogrid columns. Note some values are expressed as ranges due to tolerance stack up during fabrication.

prototypes. For all columns we used 1-mm diameter steel welding wire and the two-part plastic joints shown in Fig. 3. The wire bending was done with the D.I. Wire Pro machine [6] and the joints were printed with a Form 3 SLA printer. Note that here the joints were manually attached to the 2D unrolled lattice before it was rolled to achieve the final cylindrical geometry. After fabrication, the baseline column was spray-painted white and scanned with a 3D white light scanner (Creafom GoScan 50) to obtain a shape measurement of the initial column geometry.

B. Experimental Setup

We conducted displacement-controlled compression tests on the Bend-Formed isogrid columns using an Instron 5565 electromechanical load frame. For compatibility with the compression platens of the load frame, we fabricated flat endcaps which replicate clamped boundary conditions at each end of the column. The endcaps consisted of a circular plate with an outer ring of epoxy to hold the wire, as depicted in Fig. 5a. To keep the loading axis perpendicular to the endcaps, the columns were vertically lowered into the epoxy-filled endcaps. In addition, to minimize the effects of misalignment between the top and bottom endcaps, a marble was placed between the top compression platen and the top endcap, as shown in Fig. 5b. The marble rested in a small hole at the center of the top endcap and permitted rotation of the endcap during the compression test. This resulted in purely vertical load application and minimized the effect of tilt misalignment between the endcaps. During each compression test, a displacement of 10 mm was applied to the top endcap at a rate of 0.01 mm/s, and a video was taken of the column to characterize its deformation.

C. Finite Element Modeling

The columns shown in Fig. 4 were modeled using the finite element software Abaqus, to gain further insight into their compressive behavior. In particular, we focused on capturing the deformation and prestress of the wire lattice during rolling on the buckling and post-buckling response of the columns. To this end, the 2D lattice sketched in Fig. 2a was imported into Abaqus and meshed using linear beam elements (B31). Each element was 6.35 mm long and assigned a circular cross-section with 0.9 mm diameter, matching the cross section of the wire used to fabricate the prototypes. The elements were assigned the isotropic elastic properties of the steel wire, $E = 200$ GPa and $\nu = 0.29$. To simplify the modeling of the joints, each truss member was fully connected to its neighbors at the truss nodes, with kinematic coupling of all six degrees of freedom. The implications of this modeling choice are discussed further in the next sections.

The analysis follows multiple steps, as illustrated in Fig. 6. In the first step (Fig. 6a), the initially-flat wire lattice is rolled using rotational boundary conditions applied on its left and right boundary nodes. During this step, the edges parallel to the x -axis are constrained from moving vertically, and a series of nodes which form the centerline of the lattice

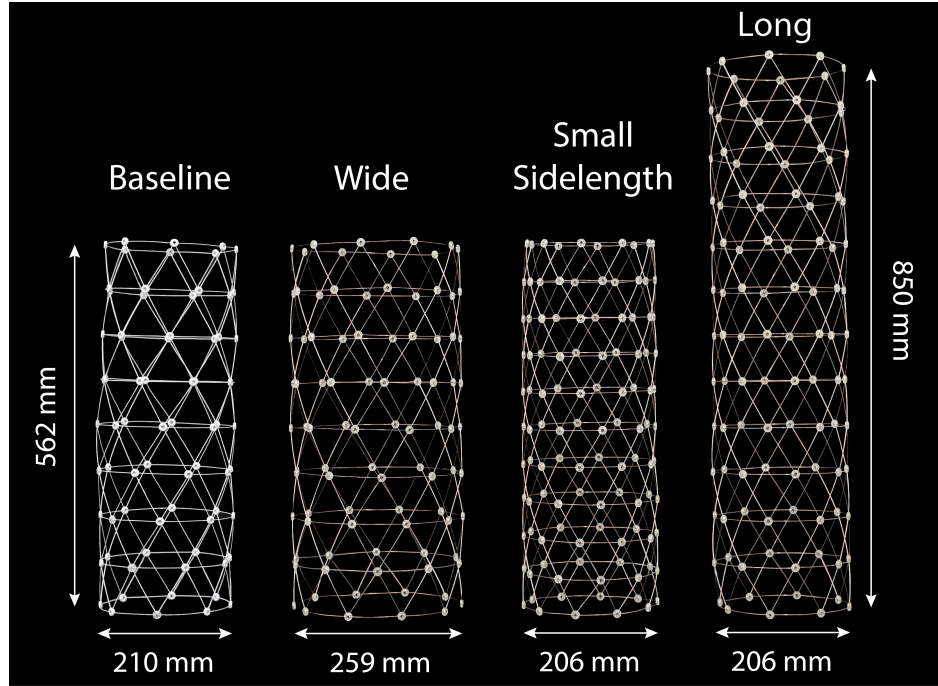


Fig. 4 Isogrid columns fabricated with Bend-Forming, using 1 mm-diameter steel welding wire and 3D printed, plastic snap-fit joints. Only one geometric parameter is varied between columns: diameter, height, or triangle sidelength. The baseline column is made from identical materials but was spray-painted white for shape measurement with a 3D white light scanner.

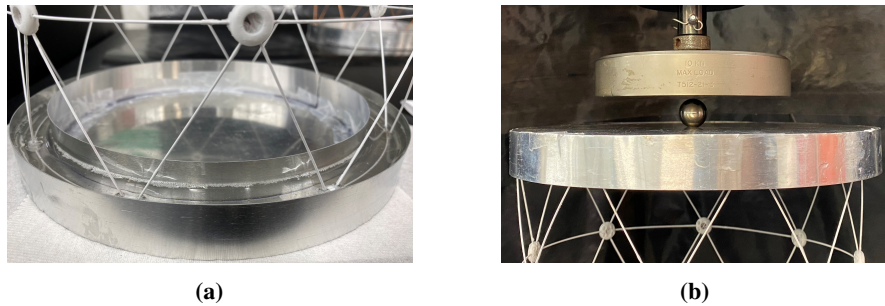


Fig. 5 (a) Epoxy-filled endcap and (b) load application with marble.

are fully clamped. The simulation is quasi-static, takes into account nonlinear geometry, and uses the Newton-Raphson solver available in Abaqus Standard. As rotations are applied to the boundary nodes, curvature and prestress develop in the wire members, and the analysis step is completed when the left and right boundary nodes are coincident.

In the second analysis step (Fig. 6b), the degrees of freedom of the left and right boundary nodes are coupled through kinematic constraints to maintain the rolled shape of the column. Physically, this corresponds to the final attachment of mechanical joints during fabrication to achieve the rolled geometry. In our simulation, these kinematic constraints are implemented through an MPC Fortran subroutine, which allows the user to define stepwise constraints which are only active after the rolling step. In addition, the same type of constraints are used to couple the top and bottom boundaries of the column to reference points along its centerline, thereby replicating the glueing of the column to the epoxy-filled endcaps. Once these additional constraints are added, the rotational boundary conditions used in the rolling step are released and the stress and deformation states are recomputed to ensure that the column is in equilibrium.

Finally, in the last analysis step (Fig. 6c), a compressive force is applied to the top reference point, which is allowed to rotate similar to the marble in the experiment. A buckling eigenvalue analysis is performed, and the full buckling and post-buckling responses are computed using a Riks solver. This particular solver uses the load magnitude as an

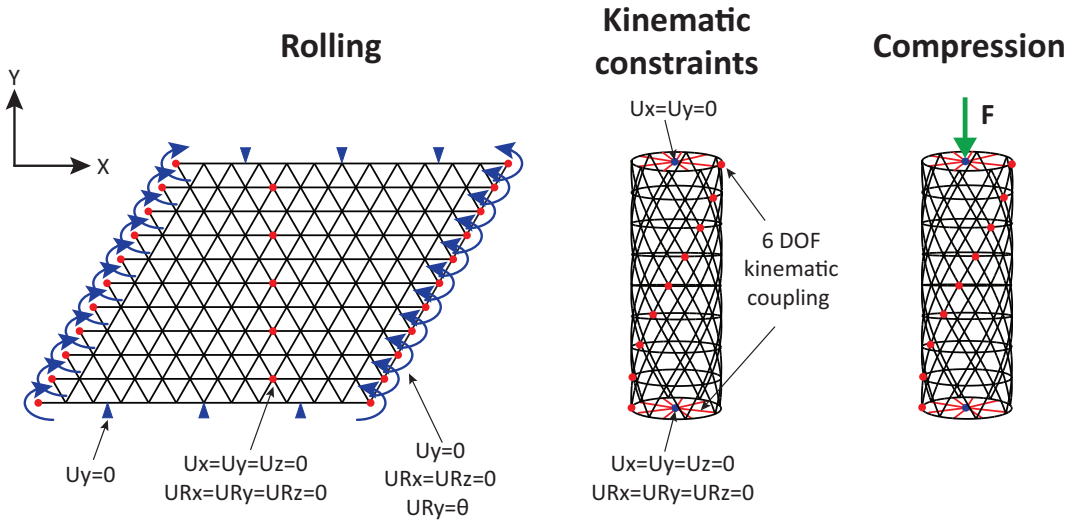


Fig. 6 Description of the finite element analysis.

additional unknown and solves simultaneously for loads and displacements. The simulation progresses by incrementing the arc-length along the static equilibrium path in load-displacement space, enabling the resolution of unstable responses. Generally for such thin shell structures, multiple post-buckling responses compete in what is referred to as “spatial chaos” [16], and geometric perturbations based on the eigenmodes of the structure are seeded in the initial geometry to guide the solver towards specific post-buckling paths. More details about this procedure are given in Section V.

IV. Results

The experimental load-displacement curves for compression of the four isogrid columns are plotted in Fig. 7, along with pictures of the columns at various points during the test. For each column, we observed an initially linear response, followed by nonlinear softening, a local maximum in load, and a region of negative stiffness. Comparing the initially linear responses of the four columns, we see that the columns with smaller side length and larger diameter (Fig. 7a, 7b) achieved both a higher axial stiffness and maximum load than the baseline column (Fig. 7c). Comparatively, the longer column (Fig. 7d) achieved both a lower axial stiffness and maximum load. These trends match with analytical expressions for axial stiffness and buckling load of isogrid columns, as derived by Mikulas [9] with effective properties of a planar triangular lattice. Table 2 lists the measured axial stiffnesses and maximum loads for the Bend-Formed columns.

After the maximum load was reached, there was a gradual decrease in load carrying capability of all columns as the compressive displacement was increased. This region of negative stiffness corresponded to the formation of localized buckling deformations or “dimples” at various locations along the height of the column. For the smaller side length and wide columns Fig. 7a, 7b), asymmetric localized deformations formed on one side of the cylinder, near the center and top bays, respectively. These dimples resulted in a large rotation of the top endcap at a displacement of 8 mm, as well as a sharp drop in load. This sharp drop in load corresponds to the conversion of strain energy into kinetic energy, an unstable behavior similar to that observed in thin-shell structures. In contrast, the baseline column showed the formation of a symmetric localized deformations at a central bay, which grew in amplitude with increasing displacement (Fig. 7c). Finally the long column showed the simultaneous formation of two localized deformations near the top and bottom bays (Fig. 7d).

V. Discussion

A. Initial geometry

To assess the imperfections in the experimentally-tested prototypes, we compared the initial geometry of the baseline column obtained from the 3D white light scanner to that predicted by the rolling step of the finite element framework

Column	k_{axial} (N/mm)	P_{\max} (N)
Baseline (D = 210 mm, H = 562 mm, SL = 82.5 mm)	68.6	187
Small side length (D = 210 mm, H = 562 mm, SL = 65 mm)	182	324
Wide (D = 259 mm, H = 562 mm, SL = 82.5 mm)	98.6	221
Long (D = 206 mm, H = 850 mm, SL = 82.5 mm)	47.5	170

Table 2 Measured axial stiffnesses and maximum loads for the four isogrid columns.

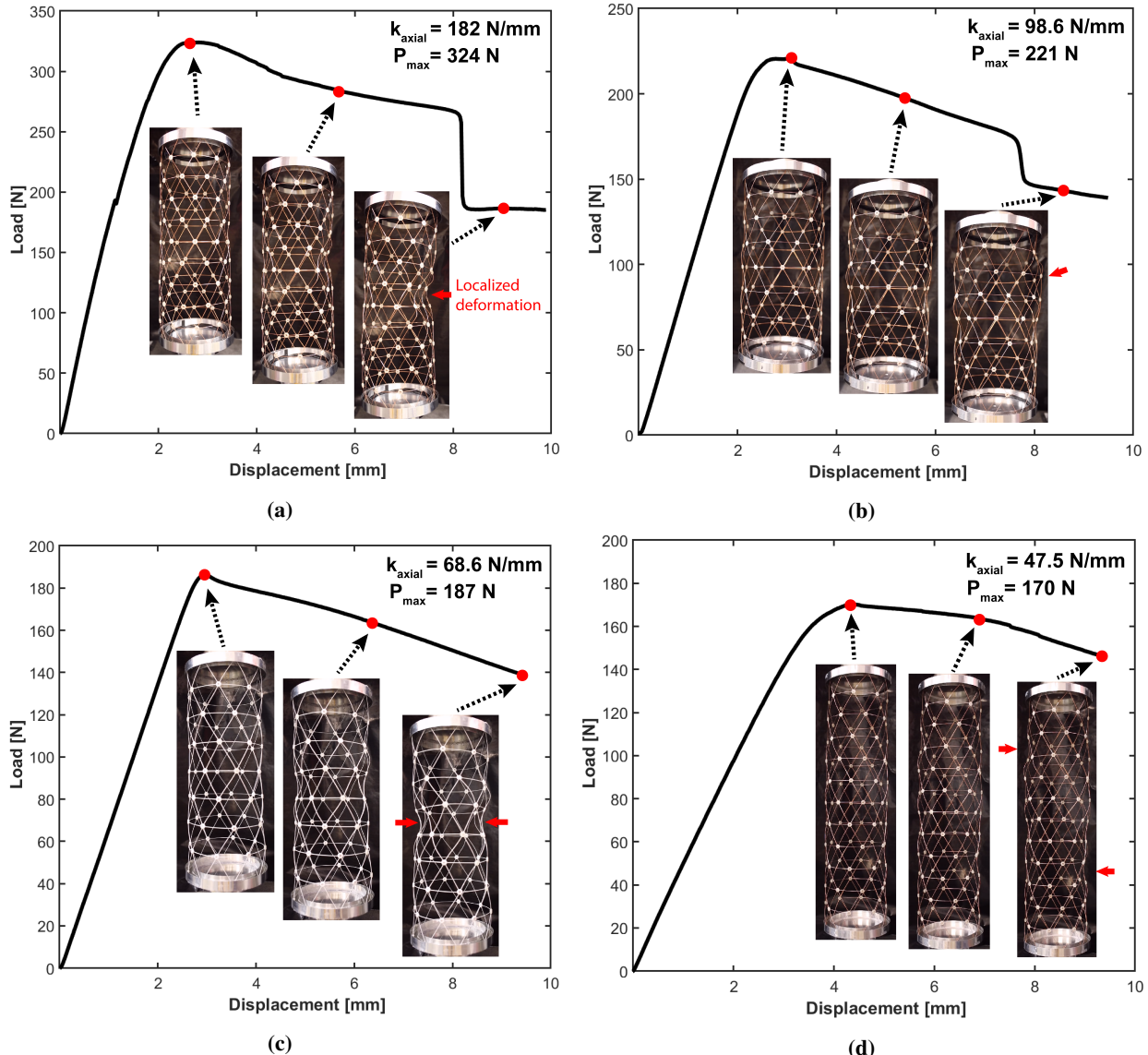


Fig. 7 Experimental results for compression tests on the four isogrid columns. For each column, the load-displacement curve is plotted with pictures of the specimen at selected points during the test. The locations of the largest-amplitude deformations are highlighted with red arrows. All four columns display an initially linear response, followed by non-linear softening, and a gradual decrease of the load which corresponds the formation of localized "dimples."

described in Section III.C. Fig. 8a shows deviations between the two geometries, mapped onto the actual column shape. Circles are fitted to both predicted and experimental mid-plane cross-sections ($H = 281$ mm), which are then used to align both columns. In the immediate vicinity of the mid-plane cross-sections, we see that shape deviations are below 1 mm. Farther from the column mid-plane, however, the deviations increase and reach a maximum at the two column extremities, on the order of 1 cm at the top end of the column. To understand this large deviation, experimental and simulated shapes are superimposed in Fig. 8a, which highlights a global twist in the structure. From this comparison, we see that most of the deviations result from a rotation of the struts along the column longitudinal axis, rather than local curvature mismatch at the wire level. Finally, a top view of the experimental column, shown in Fig. 8a, reveals an ovalization of the cross-section. These two global imperfections, twist and ovalization, may arise from the final application of joints at the boundary nodes shown in red in Fig. 6. These joints are attached to the structure after rolling, when all wire members are deformed. This process requires local flattening and clamping of the edge wires, which can introduce additional inaccuracies and angular variations between wire members at the boundary nodes. This manufacturing step may thus be responsible for the observed imperfect shape.

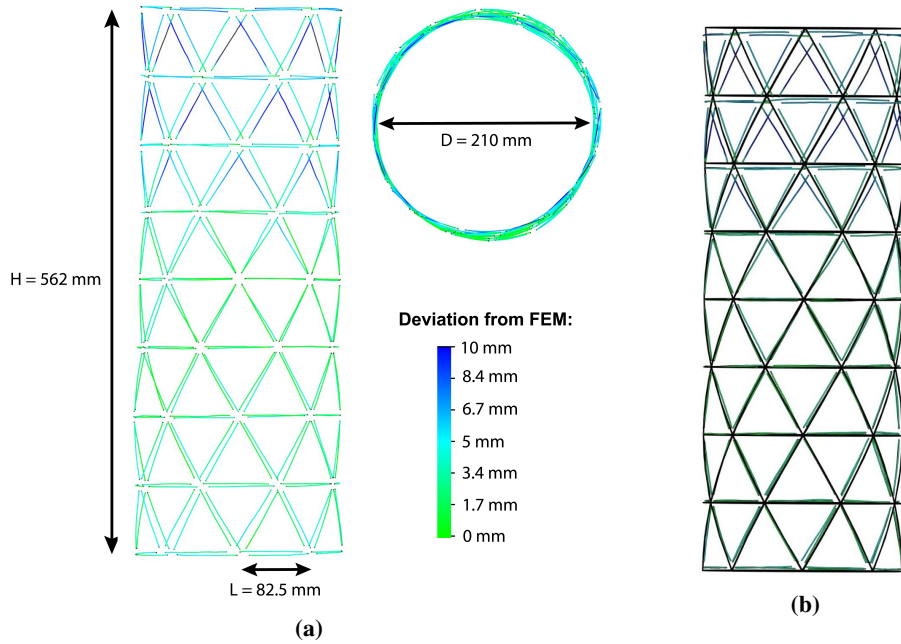


Fig. 8 a) Colormap of shape deviations between simulated and experimental shape, mapped onto the experimental geometry. **b)** Experimental and simulated shapes overlaid.

B. Buckling and post-buckling response

A classical buckling eigenvalue analysis is performed for the baseline column, linearizing the system about the origin (no compression) but including the prestress resulting from the rolling step. From this analysis three buckling eigenvalues are found under 200 N, the maximum load observed in the experiment. The first buckling eigenvalue corresponds to a critical load of 168.7 N, and the corresponding eigenmode, shown in Fig. 9a, features axisymmetric sinusoidal deformations, with a wavelength equal to twice the bay height. The second and third eigenvalues are found for a critical load of 181.9 N and 182.3 N respectively, and correspond to identical eigenmodes shown in Fig. 9a. Both modes consist of antisymmetric deformations but are rotated by 90° about the column axis.

In order to compute the load-displacement path past the first bifurcation, a geometric imperfection based on the first eigenmode is seeded into the initial geometry. This imperfection should be considered as a numerical perturbation which biases the solver at the bifurcation point, rather than a representation of the actual manufacturing imperfections [17, 18]. Several analyses are performed with different imperfection amplitudes, starting with the perfect structure. The smallest imperfection for which the load-displacement curve transitions from the perfect response to the post-buckling response with the first mode has an amplitude equal to 27% of the wire radius. The post-buckling response corresponding to this critical imperfection amplitude is shown in Fig. 10a (in blue) together with the experimental response.

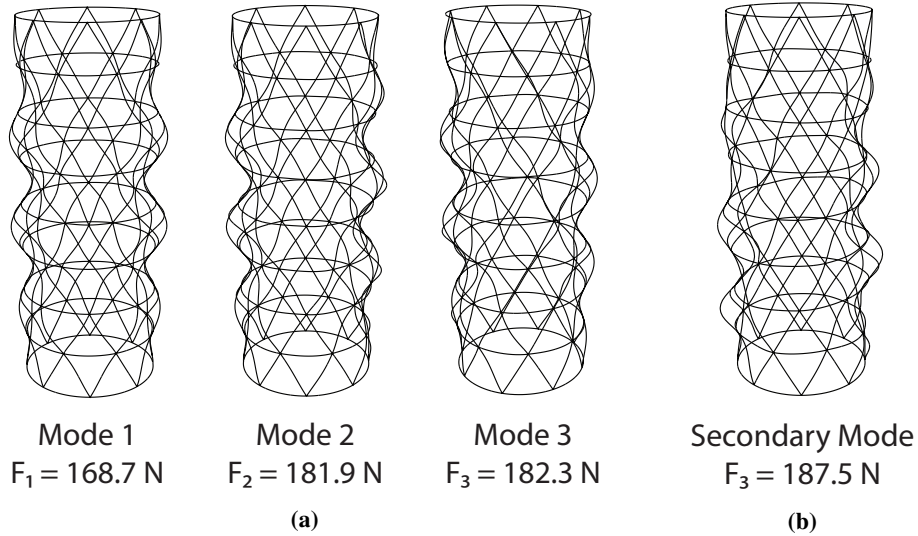


Fig. 9 a) First 3 buckling eigenmodes found under 200 N when the eigenvalue problem is linearized around the origin and b) secondary eigenmode obtained for a linearization at $F = 183 \text{ N}$.

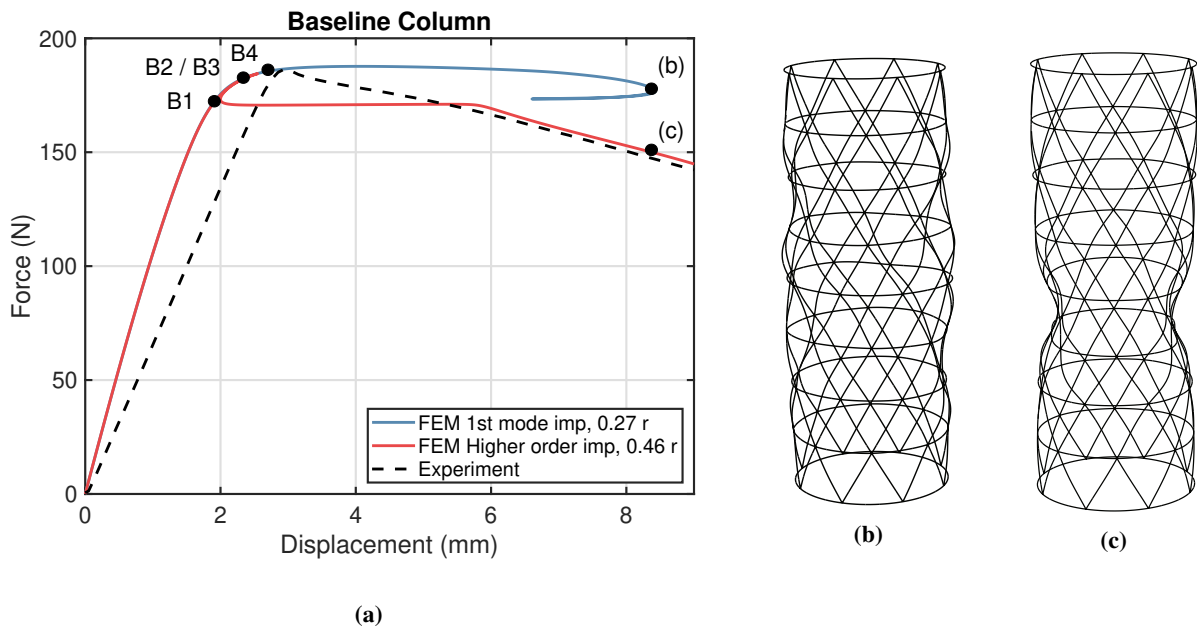


Fig. 10 (a) Comparison between responses obtained in experiment and simulation. B1, B2, B3 and B4 refer to the first, second, third, and fourth bifurcations respectively. (b) Deformed shape obtained at the end of the primary post-buckling path shown in blue and (c) deformed shape obtained at the end of the secondary post-buckling path shown in red.

In the finite element analysis, the structure first follows a weakly nonlinear load-displacement characteristic. A discrepancy in initial stiffness is observed between experiment and simulation, which can be explained by our choice of modeling the joints as full connections between wires at the truss nodes. Indeed, the axial stiffness of the column is dominated not only by the axial stiffness and flexural rigidity of the initially curved struts, but also by the compressive behavior of the joints. In the experimental specimens, only one wire runs continuously through the joint while the other wires are bent at the truss node and therefore transfer loads through the softer joint material (Fig. 3b). Preliminary

simulations (not shown here) reveal that when the resulting orthotropic joint stiffness is modeled, the overall column stiffness better matches the experimental response.

After the first bifurcation ($F_1=168.7$ N), deformations characteristic of the first eigenmode appear in the structure. The post-buckling response is stable but strongly nonlinear. Given the shape of the first eigenmode, we suspect that the column axial post-buckling stiffness depends mostly on the local bending stiffness of the truss unit cell. Past the second eigenvalue, deformations become antisymmetric and uniformly distributed on the entire column, until the maximum load is reached. This load matches well between experiment and simulation. In addition, the simulation showed that the maximum load does not depend on the imperfection amplitude, once the critical imperfection amplitude (27% of wire radius) used to trigger bifurcation is exceeded. This behavior differs significantly from the high imperfection sensitivity observed in cylindrical shells, and therefore enables a robust prediction of the maximum load the column can withstand. Past the maximum load, the structure's stiffness is negative and the load decreases slowly. This trend corresponds physically to a localization of deformations at two separate locations in the structure, as seen in Fig. 10a. At a displacement of 8.2 mm, a snap-back instability is encountered and the simulation is stopped.

By seeding the initial geometry with the first eigenmode, we observe a mismatch between the experimental and simulated post-buckling responses. In addition, the deformed shape obtained in simulation, shown in Fig. 10b, is significantly different from the shape observed in the experiment. This difference suggests that there may be additional bifurcations on the primary post-buckling path. To find them, we iteratively solve the buckling eigenvalue problem [19, 20], between the first eigenvalue and the maximum load. A secondary bifurcation is found at a critical load $F_4 = 187.5$ N, and the corresponding eigenmode is shown in Fig. 9b. The secondary eigenmode is then seeded in the structure's initial geometry, in addition to the first mode imperfection considered previously, to trace the secondary post-buckling branch stemming from this new bifurcation. A parametric study showed that a minimum imperfection amplitude of 46% of the wire radius is needed for the solver to bifurcate when the load reaches $F_4 = 187.5$ N. For this value of imperfection, we obtain the secondary post-buckling path shown in red in Fig. 10b. After the secondary bifurcation, the path becomes unstable and restabilizes at a load of 171 N, followed by a plateau. At a displacement of 5.9 mm, the load starts decreasing again and the post-buckling path follows the experimental response closely. At the end of the secondary post-buckling path, the deformed shape, shown in Fig. 10c, features symmetric deformations localized right below the column mid-plane, as observed experimentally. However, while the simulated response exhibits a snap-back after the secondary bifurcation, a gradual decrease in load is observed in the experiment. This difference in behavior may be caused by real imperfections in the structure such as the global cross-section ovalization mentioned in Section V.A. Indeed, the post-buckling shape also features a local ovalization of the cross-section, and therefore the initial imperfection is most likely the seed for this type of deformation. Since the onset of the mode is already present in the structure, the post-buckling regime consists in the amplitude growth and localization of the initial imperfection, rather than an unstable bifurcation and kinetic energy release that would be observed for a perfect structure. This reasoning also offers an explanation to why the structure would bifurcate at the secondary bifurcation rather than following the primary post-buckling path.

A similar simulation procedure was used for the three other columns to obtain their buckling and post-buckling responses. In particular, an eigenvalue analysis was carried out about the origin, and the first buckling eigenmode was seeded as imperfection in the initial shape to trace the post-buckling response. For these analyses, we did not search for additional bifurcations along the post-buckling path. The simulated post-buckling responses are shown in Fig. 11, and the relative errors in initial stiffness and maximum loads between simulation and experiment are reported in Table 3. First, we observe that the simulation consistently overpredicts the initial stiffness. This discrepancy is caused by the rigid wire connections at the truss nodes in the model, as discussed for the baseline column, which do not consider the anisotropic axial compliance of the joints. Nevertheless, an excellent match is observed between the computed and experimental maximum loads, with a relative error lower than 5% for all the columns. This observation suggests that the buckling behavior of the Bend-Formed columns is imperfection-insensitive. This can be explained by the fact that in the chosen column architecture, all wire members are initially curved and behave like beam-columns; consequently, they do not experience Euler buckling and instead follow a non-linear load-displacement behavior. A local parasitic curvature would have an effect on the load-displacement behavior of the wire, but would not cause any transition into local post-buckling. Conversely, if straight wire members were present in the column, their mechanical behavior would be different and the response would likely be more sensitive to imperfections.

We observed a good match between the deformed shapes obtained in simulation and experiment for the wide and small sidelength columns. The simulated shapes are shown in Fig. 11e and 11f. However, for the long column, the simulated deformed shapes differ from those observed experimentally (Fig. 11d): two symmetric dimples form in the simulation whereas antisymmetric deformations are observed in experiment. This observation suggests a competition

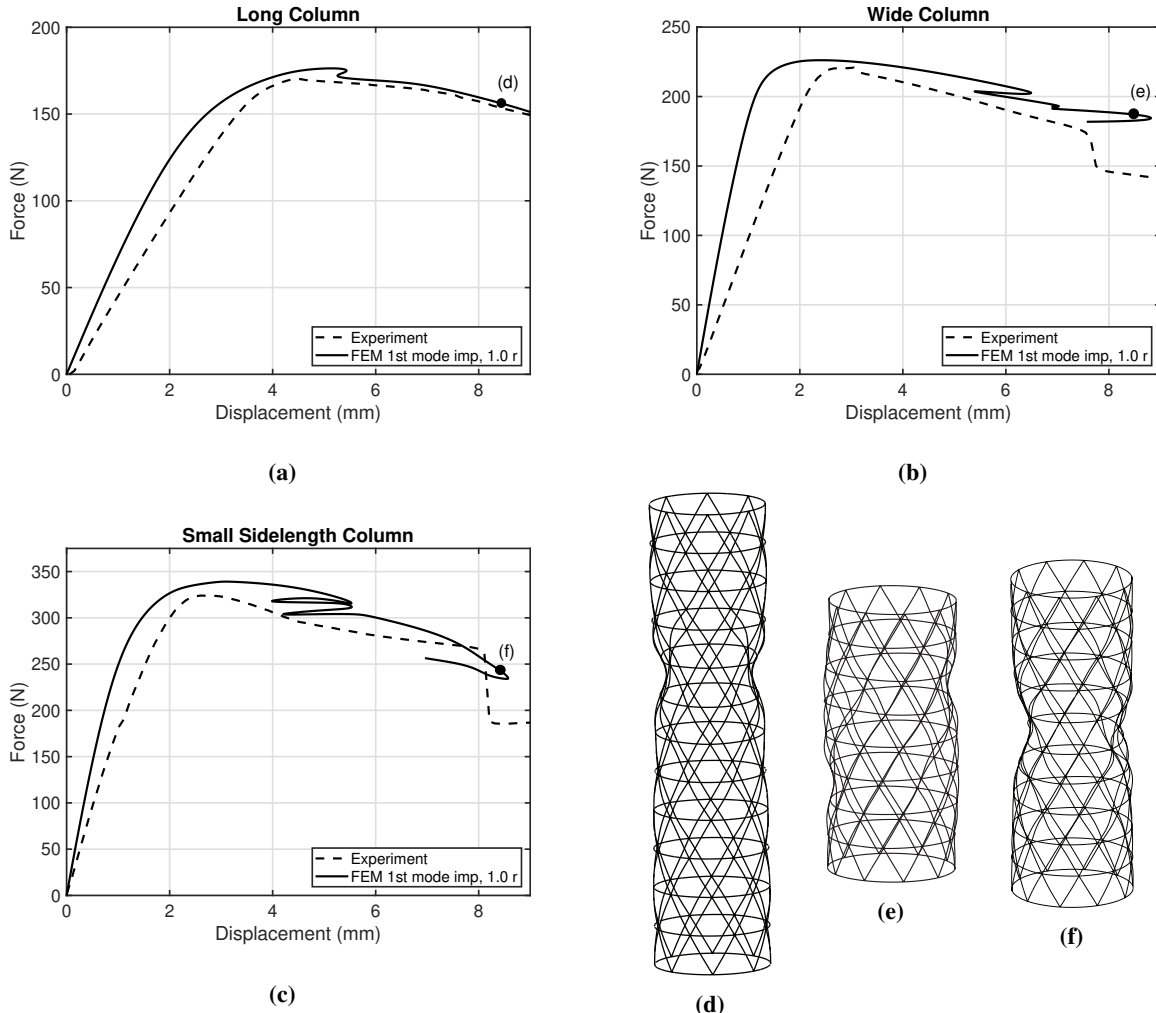


Fig. 11 Experimental and simulated load-displacement curves for the a) long column, b) wide column and c) small sidelength column. The points labeled in the figures corresponds to the deformed shapes in d), e) and f).

between buckling modes and post-buckling responses, similar to the two paths highlighted for the baseline column. To fully capture the post-buckling response and the deformed shape, an additional search for secondary bifurcations would have to be performed, as presented for the baseline column. Note that the post-buckling load-displacement characteristic is primarily driven by the number of localized buckles rather than their locations, which explains the good match between the two curves in Fig. 11a.

Beyond maximum load, the simulated long column undergoes a snap-back, which may be smoothed by imperfections in the experiment. For the wide and small sidelength columns, a series of destabilizations and restabilizations are observed, which correspond to the sequential formation of buckles in the columns. This phenomenon, termed snaking, is commonly observed in cylindrical shells [16]. The simulated post-buckling responses terminate by folding of the path, which coincides with the drop in load observed in experiment when deformations localize on one side of the column.

VI. Conclusion

Compression tests and complementary finite element analysis have been performed on reticulated isogrid columns fabricated via Bend-Forming, a low-power deformation processing technique with potential applications to in-space manufacturing. Four column prototypes, each with one geometric parameter independently varied, were axially loaded using an electromechanical load frame, and their buckling and post-buckling responses were characterized. For

Column Type	Initial stiffness relative error (%)	Maximum load relative error (%)
Baseline	56.3	0.6
Wide	107	2.4
Small side length	54.8	4.6
Long	47.9	3.6

Table 3 Relative error between experimental and simulated initial stiffness and maximum load, with respect to experimental results.

all columns, we observed an initial linear load-displacement response, followed by a highly non-linear softening, a maximum in load, and a gradual decrease in load as the displacement increased further. This negative stiffness regime corresponded physically to the localization of buckling deformations at specific locations in the structure. Finite element simulations revealed a series of bifurcations on the pre-buckling and post-buckling paths. As multiple post-buckling paths can originate from each bifurcation, we seeded the initial structures with a series of imperfections based on the buckling eigenmodes to trace the full post-buckling response. The simulations consistently over-predicted the initial stiffness due to the anisotropic axial compliance of the joints in the experimental specimens, which was not considered in our simulations. However, the simulations accurately predicted the peak load before the onset of buckling localization. The simulations showed that these specific columns are imperfection-insensitive beyond the critical imperfection amplitude threshold required to numerically trigger the post-buckling regime. Hence using a near-perfect column model enabled the accurate prediction of the maximum load, as well as the full post-buckling response and deformed shape.

Acknowledgments

The authors gratefully acknowledge financial support from Northrop Grumman Corporation and from MIT Lincoln Laboratory through the Advanced Concepts Committee. The authors also thank Dr. Sungeun Jeon of MIT Lincoln Laboratory for his assistance with the 3D scanning of the column specimen.

References

- [1] K. Taminger and R. A. Hafley, "Electron Beam Freeform Fabrication: A Rapid Metal Deposition Process," Proc. 3rd Automotive Composites Conference, September 9–10, 2003 (Troy, MI), Society of Plastics Engineers, 2003.
- [2] J. Kugler, J. Cherston, E. R. Joyce, P. Shestople, and M. P. Snyder, "Applications for the Archinaut In Space Manufacturing and Assembly Capability," presented at the AIAA SPACE and Astronautics Forum and Exposition, Orlando, FL, Sep. 2017. doi: 10.2514/6.2017-5365.
- [3] B. Levedahl et al., "Trusselator™ Technology for In-Situ Fabrication of Solar Array Support Structures," presented at the 2018 AIAA Spacecraft Structures Conference, Kissimmee, FL, Jan. 2018. doi: 10.2514/6.2018-2203.
- [4] Grumman Aerospace Corp., "Space Fabrication Demonstration System: Final Report, Technical Volume," Bethpage, NY, 1979, NASA Report N79-29213.
- [5] H. G. Bhundiya, F. Royer, and Z. Cordero, "Material and Process Considerations for In-Space Manufacturing of Large Structures," Journal of Materials Engineering and Performance, in review.
- [6] Pensa Labs, "D.I. Wire Pro Datasheet," 2020.
- [7] S. Kato, K. Abedi, P.S. Chen, F. Fan, M. Fujimoto, C. Gantes, K. Ishikawa, K. Kawaguchi, S. Kim, C. Lazaro, Y. Luo, S. Nakazawa, T. Ogawa, T. Takeuchi, Y. Taniguchi, K. Tsavdaridis, S. Xue, K. Yamamoto, and Q. Zhang, "Guide to Buckling Load Evaluation of Metal Reticulated Roof Structures," IASS WG 8, 2014.
- [8] Healey, T. (1988), "A group-theoretic approach to computational bifurcation problems with symmetry", Computer Methods in Applied Mechanics and Engineering, Volume 67, Issue 3, Pages 257-295, doi: 10.1016/0045-7825(88)90049-7.
- [9] M. M. Mikulas, "Structural Efficiency of Long Lightly Loaded Truss and Isogrid Columns for Space Applications," NASA TM-78687, 1978.
- [10] S. E. Forman and J. W. Hutchinson, "Buckling of reticulated shell structures," International Journal of Solids and Structures, vol. 6, no. 7, pp. 909–932, Jul. 1970, doi: 10.1016/0020-7683(70)90004-1.
- [11] S. P. Mai and N. A. Fleck, "Reticulated tubes: effective elastic properties and actuation response," Proc. R. Soc. A., vol. 465, no. 2103, pp. 685–708, Mar. 2009, doi: 10.1098/rspa.2008.0328.
- [12] S. Malek, T. Wierzbicki, and J. Ochsendorf, "Buckling of spherical cap gridshells: A numerical and analytical study revisiting the concept of the equivalent continuum," Engineering Structures, vol. 75, pp. 288–298, Sep. 2014, doi: 10.1016/j.engstruct.2014.05.049.
- [13] J. D. Hinkle, P. Warren, and L. D. Peterson, "Geometric Imperfection Effects in an Elastically Deployable Isogrid Column," Journal of Spacecraft and Rockets, vol. 39, no. 5, pp. 662–668, Sep. 2002, doi: 10.2514/2.3887.
- [14] D. Jungnickel, "Graphs, Networks and Algorithms," vol. 5. Berlin, Heidelberg: Springer, 2013. doi: 10.1007/978-3-642-32278-5.
- [15] V. S. Deshpande, M. F. Ashby, and N. A. Fleck, "Foam topology: bending versus stretching dominated architectures," Acta Materialia, 2001, 49(6), 1035–1040, doi: 10.1016/S1359-6454(00)00379-7.
- [16] R. M. J. Groh and A. Pirrera, "On the role of localizations in buckling of axially compressed cylinders," Proc. R. Soc. A., vol. 475, no. 2224, p. 20190006, Apr. 2019, doi: 10.1098/rspa.2019.0006.
- [17] E. Riks, "An incremental approach to the solution of snapping and buckling problems," International Journal of Solids and Structures, vol. 15, no. 7, pp. 529–551, 1979, doi: 10.1016/0020-7683(79)90081-7.
- [18] T. Rahman and E. L. Jansen, "Finite element based coupled mode initial post-buckling analysis of a composite cylindrical shell," Thin-Walled Structures, vol. 48, no. 1, pp. 25–32, Jan. 2010, doi: 10.1016/j.tws.2009.08.003.
- [19] F. Royer and S. Pellegrino, "Buckling of Ultralight Ladder-type Coilable Space Structures," presented at the AIAA Scitech 2020 Forum, Orlando, FL, Jan. 2020. doi: 10.2514/6.2020-1437.
- [20] C. Leclerc and S. Pellegrino, "Nonlinear elastic buckling of ultra-thin coilable booms," International Journal of Solids and Structures, vol. 203, pp. 46–56, Oct. 2020, doi: 10.1016/j.ijsolstr.2020.06.042.
- [21] F. Royer, "Probing the Buckling of Thin-Shell Space Structures," Dissertation (Ph.D.), California Institute of Technology, 2021, doi:10.7907/ksn2-t598.